the dc rotation simply would have provided extra suppression by a uniform amount on top of the ac oscillation suppression, as illustrated by the purple dashed curve in Fig. 3B.

As the suppressed NCRIF and the enhanced dissipation under dc rotation are thought to be coming from vortex injection, this shared common origin could be vortices. If so, the competition between vortex injection and vortex motion is one possible explanation for this crossover. A large ac oscillation amplitude causes unpinning of the vortices; the oscillatory motion of these unpinned vortices overwhelms the effect of injected quantized vortices above a certain crossover ac oscillation speed. The gradual enhancement of the crossover speed is also seen with increasing dc speed and can be attributed to the larger number of unpinned vortices that are required to observe the crossover. We note that this oscillation amplitude is still very small, orders of magnitude smaller than the critical strain for the softening of solid helium.

The appearance of extra dissipation only at low temperatures is, however, puzzling, as vortex pinning is thought to be stronger at these temperatures (*24*). The lack of similarity to better-understood superfluids and the lack of a quantitative theory for supersolid vortices makes it difficult to explain this peculiar feature.

References and Notes

1. A. J. Leggett, *Phys. Rev. Lett.* **25**, 1543 (1970).
2. E. Kim, M. H. W. Chan, *Nature* **427**, 225 (2004).
3. E. Kim, M. H. W. Chan, *Science* **305**, 1941 (2004).
4. N. Prokof'ev, *Adv. Phys.* **56**, 381 (2007).
5. J. Day, T. Herman, J. Beamish, *Phys. Rev. Lett.* **95**, 035301 (2005).
6. J. Day, J. Beamish, *Phys. Rev. Lett.* **96**, 105304 (2006).
7. A. S. C. Rittner, W. Choi, E. J. Mueller, J. D. Reppy, *Phys. Rev. B* **80**, 224516 (2009).
8. M. W. Ray, R. B. Hallock, *Phys. Rev. Lett.* **100**, 235301 (2008).
9. M. W. Ray, R. B. Hallock, *Phys. Rev. B* **79**, 224302 (2009).
10. M. W. Ray, R. B. Hallock, *Phys. Rev. B* **82**, 012502 (2010).
11. M. W. Ray, R. B. Hallock, *Phys. Rev. Lett.* **105**, 145301 (2010).
12. Y. Aoki, H. Kojima, X. Lin, *Low Temp. Phys.* **34**, 329 (2008).
13. S. Kwon, N. Mulders, E. Kim, *J. Low Temp. Phys.* **158**, 590 (2009).
14. P. W. Anderson, *Nat. Phys.* **3**, 160 (2007).
15. Z. Nussinov, A. V. Balatsky, M. J. Graf, S. A. Trugman, *Phys. Rev. B* **76**, 014530 (2007).
16. C.-D. Yoo, A. T. Dorsey, *Phys. Rev. B* **79**, 100504 (2009).
17. J. Day, J. Beamish, *Nature* **450**, 853 (2007).
18. B. Hunt *et al.*, *Science* **324**, 632 (2009).
19. I. Iwasa, *Phys. Rev. B* **81**, 104527 (2010).
20. J. D. Reppy, *Phys. Rev. Lett.* **104**, 255301 (2010).
21. P. Gumann, N. Shimizu, A. Penzev, Y. Yasuta, M. Kubota, *J. Phys. Conf. Ser.* **150**, 032026 (2009).
22. T. Obata, M. Fukuda, N. Mikhin, J. D. Reppy, M. Kubota, *J. Low Temp. Phys.* **134**, 559 (2004).
23. E. Kim, M. H. W. Chan, *Phys. Rev. Lett.* **97**, 115302 (2006).
24. H. Choi, S. Kwon, D. Y. Kim, E. Kim, *Nat. Phys.* **6**, 424 (2010).

25. Supported by the National Research Foundation of Korea through Creative Research Initiatives and the Japan Society for the Promotion of Science through a Grant-in-Aid for Scientific Research. We thank members of the Center for Supersolid and Quantum Matter Research, in particular D. Y. Kim and S. Kwon, for helpful discussions.

12 August 2010; accepted 8 November 2010
Published online 18 November 2010;
10.1126/science.1196409

In Situ Observation of the Electrochemical Lithiation of a Single SnO_2 Nanowire Electrode

Jian Yu Huang,[1]* Li Zhong,[2] Chong Min Wang,[3]* John P. Sullivan,[1]* Wu Xu,[4] Li Qiang Zhang,[2] Scott X. Mao,[2]* Nicholas S. Hudak,[1] Xiao Hua Liu,[1] Arunkumar Subramanian,[1] Hongyou Fan,[5] Liang Qi,[6,7] Akihiro Kushima,[7] Ju Li[6,7]*

We report the creation of a nanoscale electrochemical device inside a transmission electron microscope—consisting of a single tin dioxide (SnO_2) nanowire anode, an ionic liquid electrolyte, and a bulk lithium cobalt dioxide ($LiCoO_2$) cathode—and the in situ observation of the lithiation of the SnO_2 nanowire during electrochemical charging. Upon charging, a reaction front propagated progressively along the nanowire, causing the nanowire to swell, elongate, and spiral. The reaction front is a "Medusa zone" containing a high density of mobile dislocations, which are continuously nucleated and absorbed at the moving front. This dislocation cloud indicates large in-plane misfit stresses and is a structural precursor to electrochemically driven solid-state amorphization. Because lithiation-induced volume expansion, plasticity, and pulverization of electrode materials are the major mechanical effects that plague the performance and lifetime of high-capacity anodes in lithium-ion batteries, our observations provide important mechanistic insight for the design of advanced batteries.

Lithiation and delithiation of the electrode materials in lithium-ion batteries (LIBs) induce large strains in the host material, leading to plasticity and fracture. Lithiation is also often accompanied by phase transformations, such as electrochemically driven solid-state amorphization (ESA) (*1*). These electrochemical reaction–induced microstructural events limit the energy capacity and cycle lifetime of LIBs (*2*–*6*). It was recently reported that lithium-ion anode materials composed of nanowires (*7*–*12*) can offer improved performance and lifetime relative to those of micrometer-scale or larger materials. The improvements are often attributed to the nanowire's unique geometry and enhanced accommodation of the transformation strains that occur during cycling (*9*, *10*, *13*, *14*). However, the detailed mechanisms of strain-induced plasticity and strain accommodation in nanowires during electrochemical charging are largely unknown.

We have successfully constructed a nanoscale electrochemical device consisting of a single SnO_2 nanowire as an anode, an ionic liquid–based electrolyte (ILE), and a cathode of $LiCoO_2$ particles inside a high-resolution transmission electron microscope (HRTEM) (Fig. 1A) to enable direct real-time visualization of electrochemical reaction–induced microstructural changes. As shown in Fig. 1B, the initial SnO_2 nanowire was straight with a smooth surface morphology. After contact with the ILE, the ILE wicked up the nanowire, forming a meniscus (Fig. 1C). Potential was then applied to the SnO_2 nanowire at –3.5 V with respect to the $LiCoO_2$ counterelectrode. This initiated an electrochemical reaction at the point of contact between the SnO_2 nanowire and the ILE where reduction of the SnO_2 was observed. This solid-state reaction front propagated along the longitudinal direction of the nanowire away from the electrolyte (Fig. 1, D to S, and movie S1). As the reaction front propagated, the diameter and length of the nanowire increased, and the TEM image contrast changed from typical crystalline diffraction contrast to a gray, mostly featureless contrast typical of amorphous materials (Fig. 2 and Fig. 3). At 625 s (Fig. 1, I and P to S, and movie S1), the nanowire began to flex rapidly, which resulted in the formation of a bend and the start of a coil of a spiral. After 1860 s of charging, the initially straight nanowire (Fig. 1B) exhibited a twisted and meandering morphology (Fig. 1O), indicative of extensive plastic deformation and microstructural changes. It took about half an hour to charge a nanowire with initial length of 16 μm and diameter of 188 nm. After charging, this nanowire had elongated ~60%, the diameter expanded ~45%, and the total volume expanded about 240%.

[1]Center for Integrated Nanotechnologies, Sandia National Laboratories, Albuquerque, NM 87185, USA. [2]Department of Mechanical Engineering and Materials Science, University of Pittsburgh, Pittsburgh, PA 15261, USA. [3]Environmental Molecular Sciences Laboratory, Pacific Northwest National Laboratory, Richland, WA 99354, USA. [4]Energy and Environment Directorate, Pacific Northwest National Laboratory, Richland, WA 99354, USA. [5]Advanced Materials Lab, Sandia National Laboratories, Albuquerque, NM 87106, USA. [6]State Key Laboratory for Mechanical Behavior of Materials and Frontier Institute of Science and Technology, Xi'an Jiaotong University, Xi'an 710049, China. [7]Department of Materials Science and Engineering, University of Pennsylvania, Philadelphia, PA 19104, USA.

*To whom correspondence should be addressed. E-mail: jhuang@sandia.gov (J.Y.H.); chongmin.wang@pnl.gov (C.M.W.); jpsulli@sandia.gov (J.P.S.); sxm2@pitt.edu (S.X.M.); liju@seas.upenn.edu (J.L.)

The large shape change of the nanowire during charging was a general feature of all the nanowires that were investigated. In fig. S1, A to K, we show the structural changes of another SnO_2 nanowire before and after charging, in this case polarized to −4 V with respect to the $LiCoO_2$ cathode. It took about 80 min to charge this nanowire with an initial length of 14 μm and diameter of 107 nm. After charging, the initially straight nanowire became highly distorted, with a total elongation of 90%, a diameter expansion of 35%, and a total volume expansion of 250%. Figure S2 shows the charging dynamics of a third nanowire. Large shape changes were observed again.

Figure 2 shows a more detailed structure and phase characterization of the nanowire before and after charging. Close inspection of the reaction front (Fig. 2A) revealed the presence of a region of a high density of dislocations separating the nonreacted and reacted segments of the nanowire. Before reaction, the nanowire was straight and monocrystalline, as revealed by the electron diffraction pattern (EDP) (Fig. 2B). Immediately after charging, the nanowire showed a dark gray contrast (Fig. 2A), and the EDP of most areas showed amorphous haloes (Fig. 2D). After prolonged charging, the nanowire comprised small nanocrystals dispersed in an amorphous matrix (Fig. 2F), and the EDP showed diffraction rings superimposed on diffuse amorphous haloes (Fig. 2E); the diffraction rings could be indexed as hexagonal Li_xSn (orange indices in Fig. 2E) and tetragonal Sn (black indices in Fig. 2E). The EDP from the reaction front (Fig. 2C) showed diffraction spots superimposed on a diffuse scattering background. These diffraction spots are similar to that of the nonreacted nanowire, except that the zone axis of the former is slightly tilted with respect to the latter. Electron energy loss spectroscopy (EELS) indicated that, after reaction, the nanowire contained metallic Sn, Li, and Li_2O (Fig. 2, G and H). EELS from a charged segment of the nanowire, such as that shown in Fig. 2A, showed the presence of Li (Fig. 2G, red line profile). The Li-K edge is similar to that of Li_2O rather than metallic Li (*15*), indicating that the amorphous phase is Li_2O. Occasionally, an EDP revealed the presence of nanocrystalline Li_2O, which was found in the nanowire after charging (fig. S3). These results revealed that the nanowire after charging consists of nanocrystalline Li_xSn and Sn particles dispersed in an amorphous Li_2O matrix.

In total, these measurements reveal that when a SnO_2 nanowire was polarized at a sufficiently negative potential with respect to $LiCoO_2$, the SnO_2 was initially reduced to nanocrystalline Sn

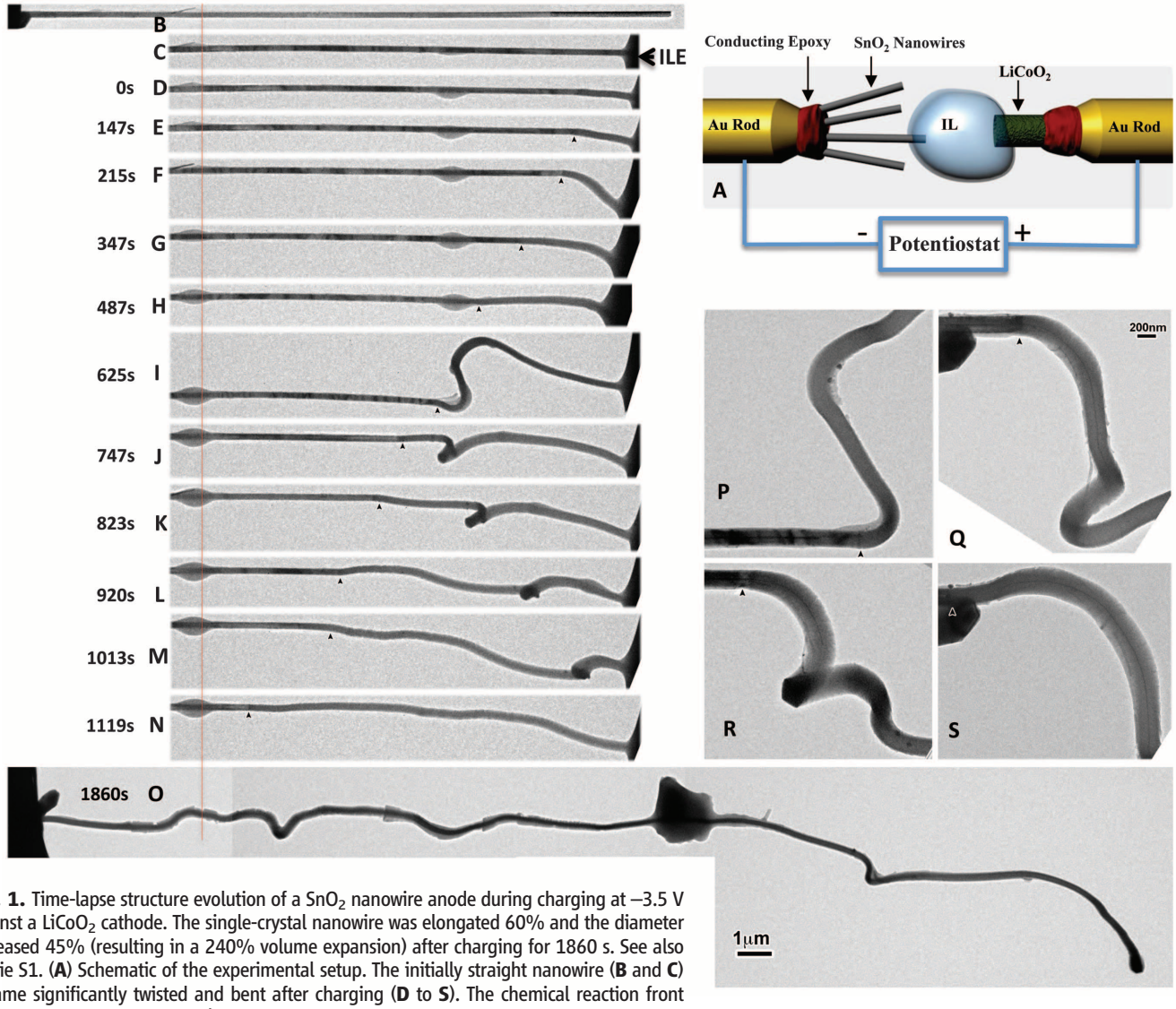

Fig. 1. Time-lapse structure evolution of a SnO_2 nanowire anode during charging at −3.5 V against a $LiCoO_2$ cathode. The single-crystal nanowire was elongated 60% and the diameter increased 45% (resulting in a 240% volume expansion) after charging for 1860 s. See also movie S1. (**A**) Schematic of the experimental setup. The initially straight nanowire (**B** and **C**) became significantly twisted and bent after charging (**D** to **S**). The chemical reaction front progressed along the nanowire's longitudinal direction, with the front clearly visible, as pointed out by arrowheads in (E) to (S). The red line in (B) to (O) marks a reference point to track the change of the nanowire length. (P) to (S) are sequential high-magnification images showing the progressive migration of the reaction front, swelling, and the twisted morphology of the nanowire after the reaction front passed by. The big dark particle in the middle of (O) is an island of gelled ILE. Because of the long cumulative electron beam exposure time during the recording of TEM images, the ILE front became gelled (with high viscosity) at this spot.

and amorphous Li_2O, which suggests the following reduction reaction: $4Li^+ + SnO_2 + 4e^- \rightarrow 2Li_2O + Sn$. This is the "forming stage" to produce a Sn-containing anode. After this initial phase transformation, the operation of the Sn-$LiCoO_2$ battery is based on a reversible reaction, such as $Sn + x\,Li^+ + x\,e^- \leftrightarrow Li_xSn$ ($0 \le x \le 4.4$) (*16*). While reduction was occurring at the SnO_2 nanowire anode, at the $LiCoO_2$ cathode Co was being oxidized from Co^{3+} to Co^{4+}, and Li^+ ions were expelled; that is, $LiCoO_2 \rightarrow Li_{1-\delta}CoO_2 + \delta\,Li^+ + \delta\,e^-$.

In contrast to bulk SnO_2, which is a brittle ceramic, nanowire SnO_2 showed large plasticity (as evidenced by the high dislocation density at the reaction front), and we did not observe fracture or cracking despite the high strain at the reacting interface. Details of the generation and migration of the dislocations near the reacting interface are shown in Fig. 3 and movies S2 to S5. In SnO_2, the width of this region of high dislocation density was ~10^2 nm, and is named the "Medusa zone" because of the appearance of dislocations "snaking" away from the interface. It may occur in certain electrochemical solid-state reactions, and its existence indicates very high stresses at the reaction front; the high stress drives dislocation nucleation and motion. Previously, ex situ TEM studies showed that a high density of dislocations may exist in $LiCoO_2$ cathodes in LIBs as a result of electrochemical cycling (*17*). However, it is far from clear when and how these dislocations are generated and how they evolve during cycling. Our in situ movies show that the dislocations were continuously nucleated in the crystal regions and then moved away from the highly stressed region. They were also pursued from behind and absorbed by the moving amorphous-crystalline interface (ACI) (*18*), thereby maintaining a steady state in the total dislocation cloud, which migrated in an approximate chevron shape along the nanowire. One type of dislocation in SnO_2 is determined to be of $[01\bar{1}](100)$ slip character (fig. S4). We have performed ab initio density functional theory (DFT) calculations and found the ideal shear strength of SnO_2 to be ~10 GPa. Because a very high density of dislocations was seen to be nucleated readily and continuously at the interface even as the old nucleation zone was being demolished by the advancing reaction front (which would imply the removal of the original Frank-Read dislocation sources), we postulate that

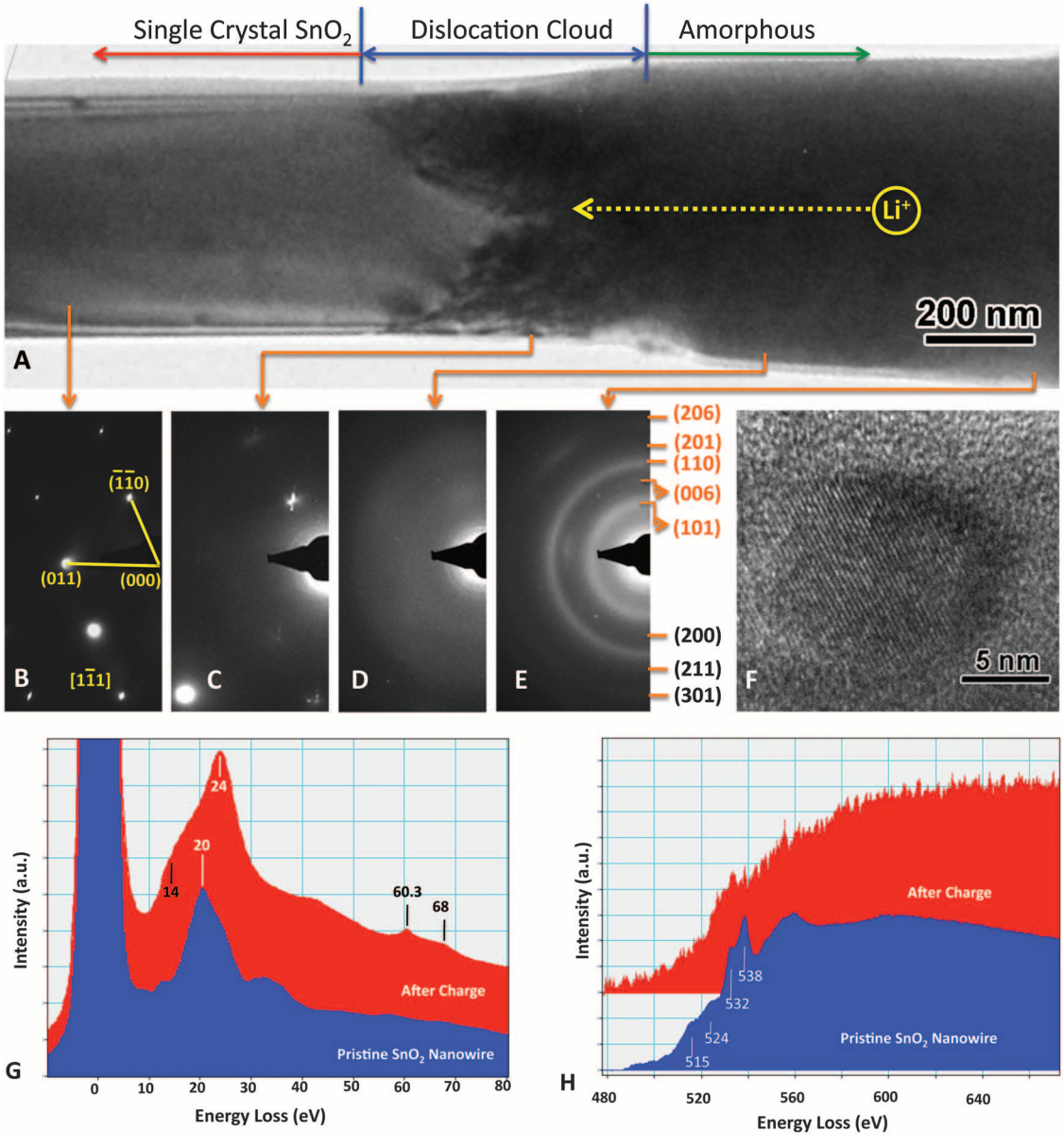

Fig. 2. Structural and phase characterization of another SnO_2 nanowire anode during charging at −3.5 V against the $LiCoO_2$ cathode. (**A**) TEM micrograph of the nanowire containing a reaction front ("dislocation cloud") separating the reacted ("amorphous") and nonreacted ("single-crystal SnO_2") sections. (**B** to **E**) EDPs from the different sections of the nanowire. The pristine nanowire was single crystalline and the corresponding EDP (B) can be indexed as the $[1\bar{1}1]$ zone axis of rutile SnO_2. The EDP from the dislocation zone (C) shows a spot pattern superimposed on a diffuse scattering background. The EDP from an area immediately after the reaction front (D) shows an amorphous halo. The EDP from an area far away from the reaction front (E) shows diffraction rings superimposed on a diffuse amorphous halo. The diffraction rings can be indexed as tetragonal Sn (black indices) and a Li_xSn compound such as hexagonal $Li_{13}Sn_5$ (orange indices). (**F**) A HRTEM image from a charged nanowire showing Sn nanoparticles dispersed in an amorphous matrix. (**G** to **H**) Low-loss and core-loss EELS from a large area of the nanowire after reaction (red line profile) and a pristine nanowire (blue line profile). The pristine SnO_2 shows two characteristic core-loss peaks at 515 and 524 eV, corresponding to the Sn-$M_{4,5}$ edge riding on a delayed edge. The peaks at 532 and 538 eV arise from the O-K edge. Note that Li is present in the charged nanowire (G). The plasmon loss peaks at 20 eV, 24 eV, and 14 eV are in excellent agreement with SnO_2, Li_2O, and pure Sn, respectively.

a stress close to the ideal strength (*14*) should exist in the Medusa zone. Such a large stress would be expected at the reaction interface, as the reacted side of the interface exhibits a 45% increase in radial expansion relative to the unreacted side. This would generate a large tensile stress near the ACI that leads to spontaneous dislocation nucleation on the unreacted side, and a large compressive stress on the reacted amorphous side. Plasticity is expected to also occur on the amorphous side (*18*, *19*), despite the lack of dislocations.

We note two important consequences of the observed dislocation structure and dynamics at the reacting interface. First, the dislocation cores may be highly effective Li transport channels (*20*) and may facilitate Li ion insertion into the crystalline interior, effectively increasing the reaction kinetics. Second, the amorphous phase we observed in situ did not form via the melt-quench mechanism, but via a direct crystal-to-glass transition (i.e., ESA) (*1*). Solid-state amorphization (*21*–*23*) has often been associated with mechanical alloying of bulk materials (e.g., ball-milling) (*24*–*26*). Here it is observed in the context of an electrochemical reaction with large stress and apparent dislocation plasticity at the reaction front. Fortunately, electron transparency allows us to capture the dynamical process of ESA with TEM. Our observations suggest that stress-driven dislocation plasticity may be a precursor to some solid-state amorphizations (*23*–*26*). The dislocation density we observed in the Medusa zone was exceptionally high, on the order of $10^{17}/m^2$, which is about two orders of magnitude larger than that in heavily work-hardened face-centered cubic metals (*27*). Such a high dislocation density was caused by the exceptionally high stress driven by the electrochemical reaction. The dislocation cloud disturbs the structural order of the crystal and drives it far from equilibrium. This can provide the necessary energy and kinetic pathway toward complete amorphization.

In addition to the interesting precipitate/dislocation microstructures, we observed very unusual gross morphological changes of the nanowire. Elastic energy strongly influences the shape of phase transformation products (*28*), and the nanowire geometry provides an elasticity boundary condition very different from that of 3D bulk materials. For the SnO_2 nanowire polarized at –4 V versus $LiCoO_2$ (fig. S1), we observed a very large anisotropy in the transformation strain, namely ~90% elongation in the ⟨011⟩ axial direction compared to ~35% expansion in the transverse directions; the total volume expanded by ~250%. Our DFT calculation gives a net volume expansion that matches very well with the experimental result (table S1), assuming $x = 3$ in the charging reaction $(4 + x)Li^+ + SnO_2 + (4 + x)e^- \rightarrow 2Li_2O + Li_xSn$. But the calculated transformation strain anisotropy, based on uniform electrochemical Li^+ insertions alone, is completely different; that is, the largest expansion should occur along ⟨001⟩ instead of ⟨011⟩. We interpret this contrast as due to the buckling instability of the nanowire (movie S1); the wire is elastically very compliant in the axial direction and therefore prefers to accommodate the volume expansion in the axial direction. In the transverse directions, because of geometric con-

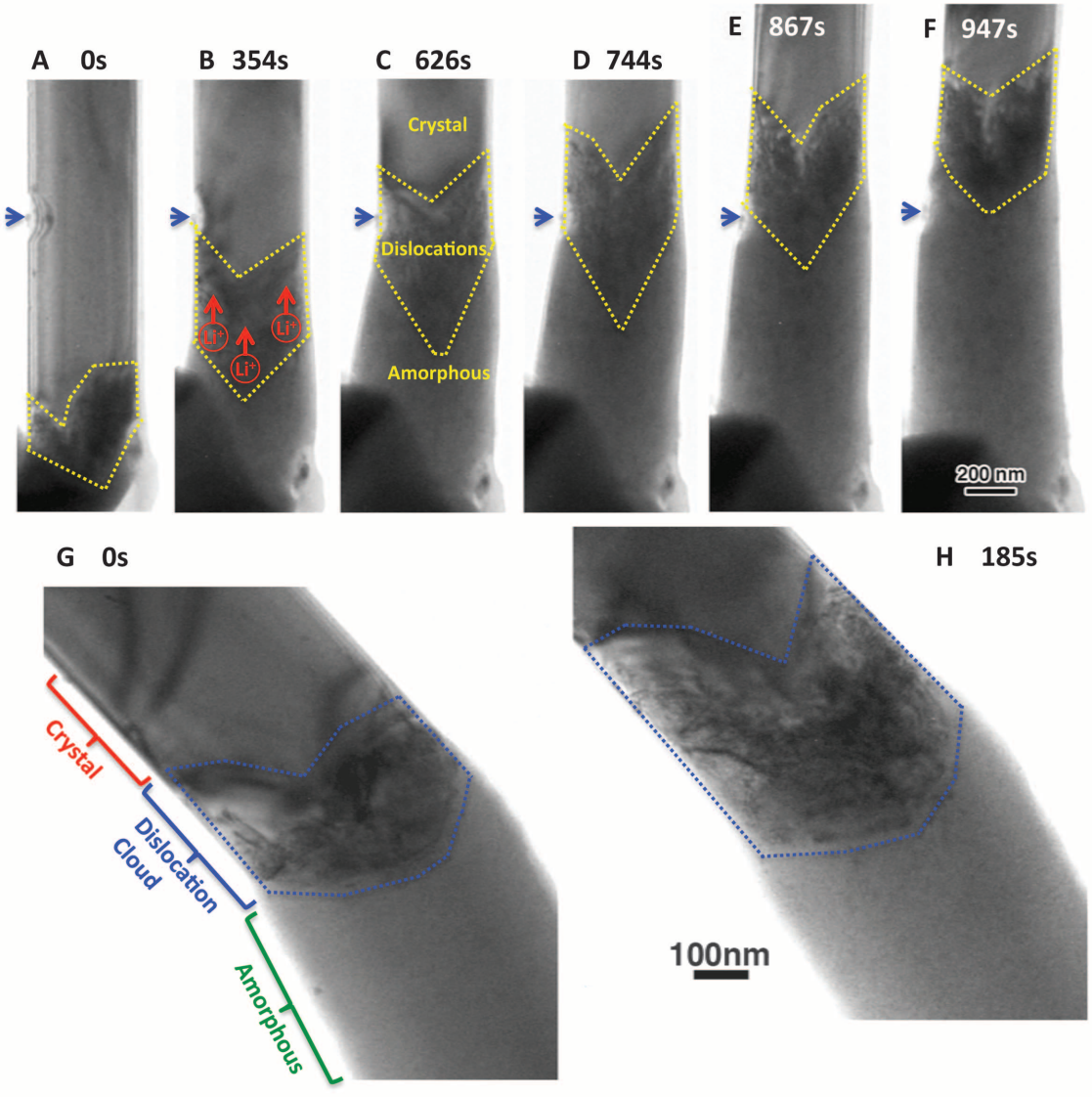

Fig. 3. TEM images revealed a high density of dislocations emerging from the reaction front (marked by chevron-shaped dotted lines). As the dislocation front propagated, the crystalline contrast changed to gray amorphous contrast instantaneously, and the nanowire diameter increased immediately. See also movies S2 to S5. (**A** to **F**) and (**G** and **H**) Two sets of time-lapsed TEM images showing the high density of dislocations that appeared at the reaction front and the migration of the reaction front.

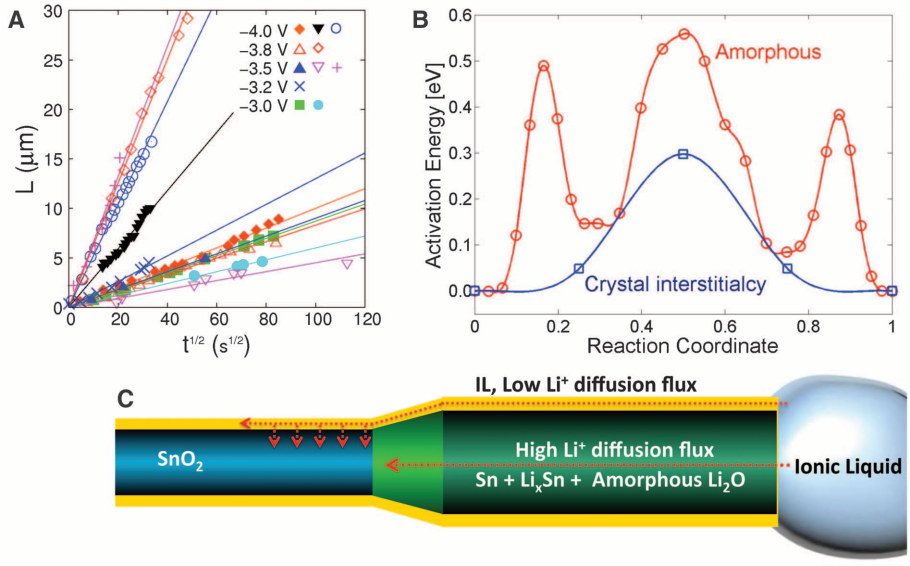

Fig. 4. (**A**) Plot of the reaction front migration distance *L* versus the square root of time for 11 nanowires. (**B**) Representative Li^+ migration energy barrier in crystalline and amorphous Li_2O from DFT calculations. (**C**) Schematic drawing showing the high Li diffusion flux in Li_2O.

straints at the ACI, large in-plane stresses develop that drive mechanical plasticity. The net shape change of the nanowire observed is therefore not due to lithiation alone, but is the combined outcome of electrochemical-mechanical actions, where stress-induced plasticity plays an important part (fig. S5). These shape-change features mean that the design and packaging of nanowire nanobatteries must take into account the large conformation changes of the nanowire (buckling, coiling, and twisting) without breaking electrical contact or shorting across electrodes. It is also noteworthy that among the several nanowires we charged and discharged, none of them fractured despite the large strain and conformational changes. This is further testimony to the mechanical robustness associated with the nanowire geometry relative to bulk ceramic electrodes (*13*, *14*).

The displacement of the reaction front versus the square root of reaction time is plotted in Fig. 4A using the results of 11 experiments. The nearly parabolic behavior indicates the importance of long-range Li^+ diffusion (Fig. 4C). On the basis of our data, the diffusivity of Li^+ in the reacted amorphous sections ranges from 5×10^{-16} to 5×10^{-14} m^2/s, which is of the same range as the results reported for bulk Li_2O (*29*–*31*) if extrapolated to room temperature. The somewhat large scattering in diffusivity value is reasonable, because unlike a crystal, the amorphous atomic structure is not unique, and slightly different formation conditions (for example, due to different local voltage) of the amorphized nanowire can lead to different diffusivities. The characteristic migration energy barrier of ~0.4 eV (Fig. 4B), obtained from our ab initio calculations using an ensemble of Li^+ migration paths in Li_2O with approximately the same initial and final potential energies, matches our experimental diffusivities reasonably well. Note that the wetting layer of ILE on the nanowire surface is so thin (less than 10 nm) that the flux of Li^+ transported by this layer is outmatched by the flux from solid-state diffusion in the amorphous Li_2O reaction product. This explains why the reaction occurred along the longitudinal direction rather than along the radial direction.

To imitate the scenario in a real battery configuration, we have also conducted experiments with the nanowire partially immersed in the ILE to see whether there is any difference in the post-charging shape changes between the immersed segments and the exposed segments of the nanowire (fig. S6). We found no essential difference in the final shape between the two different segments of the nanowire, both of which show large shape changes with extensive buckling and spiraling (fig. S6).

After charging, we also performed discharge, and TEM showed that the Li_xSn alloy nanoparticles were converted back to pure Sn (fig. S7) and that the diameter of the nanowire decreased. The overall volume change during discharge was much less than during the initial charging process, however. During initial charging, the formation of Li_2O caused large volume expansion [irreversible (*16*)], whereas in the discharging process, the Li_2O glass did not participate in the electrochemical reaction and only the Li_xSn nanoprecipitates, which occupy smaller volume, were active. Although the successful charging and discharging demonstrate that this system constitutes a working electrochemical device (*32*), we were unable to quantify the reversible capacity of this device because the low discharge current (estimated to be less than 3 pA) was much lower than our noise floor for our electrical current measurement.

The methodology described above should stimulate real-time studies of the microscopic processes in batteries and lead to a more complete understanding of the mechanisms governing battery performance and reliability, especially those properties that are controlled by microstructure. Although the work was carried out using SnO_2 nanowires, these experiments can be extended to other materials, for either cathode or anode studies. Further, autonomous nanomachines such as nanorobots (*33*) call for extreme miniaturization of power supplies (*34*) with energy generation (*35*) and energy storage functions. The concept of a stand-alone rechargeable nanobattery that uses individual nanowires as electrodes and a nanoscale electrolyte is quite appealing. Although our work falls short of realizing a fully packaged nanobattery, we believe that the in situ characterization and modeling reported here is an important step toward achieving that goal.

References and Notes

1. P. Limthongkul, Y. I. Jang, N. J. Dudney, Y. M. Chiang, *Acta Mater.* **51**, 1103 (2003).
2. A. K. Padhi, K. S. Nanjundaswamy, J. B. Goodenough, *J. Electrochem. Soc.* **144**, 1188 (1997).
3. J. M. Tarascon, M. Armand, *Nature* **414**, 359 (2001).
4. Y. Shao-Horn, L. Croguennec, C. Delmas, E. C. Nelson, M. A. O'Keefe, *Nat. Mater.* **2**, 464 (2003).
5. B. Kang, G. Ceder, *Nature* **458**, 190 (2009).
6. W. Lai *et al.*, *Adv. Mater.* **22**, E139 (2010).
7. K. T. Nam *et al.*, *Science* **312**, 885 (2006); 10.1126/science.1122716.
8. M. S. Park *et al.*, *Angew. Chem. Int. Ed.* **46**, 750 (2007).
9. C. K. Chan *et al.*, *Nat. Nanotechnol.* **3**, 31 (2008).
10. H. Kim, J. Cho, *Nano Lett.* **8**, 3688 (2008).
11. Y. D. Ko, J. G. Kang, J. G. Park, S. Lee, D. W. Kim, *Nanotechnology* **20**, 455701 (2009).
12. A. Magasinski *et al.*, *Nat. Mater.* **9**, 353 (2010).
13. T. K. Bhandakkar, H. J. Gao, *Int. J. Solids Struct.* **47**, 1424 (2010).
14. T. Zhu, J. Li, *Prog. Mater. Sci.* **55**, 710 (2010).
15. D. R. Liu, D. B. Williams, *Philos. Mag. B* **53**, L123 (1986).
16. I. A. Courtney, J. R. Dahn, *J. Electrochem. Soc.* **144**, 2045 (1997).
17. H. Gabrisch, R. Yazami, B. Fultz, *Electrochem. Solid State Lett.* **5**, A111 (2002).
18. Y. M. Wang, J. Li, A. V. Hamza, T. W. Barbee Jr., *Proc. Natl. Acad. Sci. U.S.A.* **104**, 11155 (2007).
19. Z. W. Shan *et al.*, *Phys. Rev. B* **77**, 155419 (2008).
20. M. Legros, G. Dehm, E. Arzt, T. J. Balk, *Science* **319**, 1646 (2008).
21. D. Wolf, P. R. Okamoto, S. Yip, J. F. Lutsko, M. Kluge, *J. Mater. Res.* **5**, 286 (1990).
22. H. J. Fecht, *Nature* **356**, 133 (1992).
23. H. Bakker, G. F. Zhou, H. Yang, *Prog. Mater. Sci.* **39**, 159 (1995).
24. C. Suryanarayana, *Prog. Mater. Sci.* **46**, 1 (2001).
25. J. Y. Huang, H. Yasuda, H. Mori, *Philos. Mag. Lett.* **79**, 305 (1999).
26. J. Y. Huang, Y. T. Zhu, X. Z. Liao, R. Z. Valiev, *Philos. Mag. Lett.* **84**, 183 (2004).
27. H. Mughrabi, *Philos. Mag.* **86**, 4037 (2006).
28. A. G. Khachaturyan, *Theory of Structural Transformations in Solids* (Wiley, New York, 1983).
29. H. Ohno *et al.*, *J. Nucl. Mater.* **118**, 242 (1983).
30. T. Oda, S. Tanaka, *J. Nucl. Mater.* **386–388**, 1087 (2009).
31. J. Habasaki, Y. Hiwatari, *Phys. Rev. B* **69**, 144207 (2004).
32. A. Brazier *et al.*, *Chem. Mater.* **20**, 2352 (2008).
33. K. Kostarelos, *Nanomedicine* **5**, 341 (2010).
34. A. E. Curtright, P. J. Bouwman, R. C. Wartena, K. E. Swider-Lyons, *Int. J. Nanotechnol.* **1**, 226 (2004).
35. Z. L. Wang, J. Song, *Science* **312**, 242 (2006).

36. J.Y.H. thanks K. Xu for valuable discussions. Supported by a Laboratory Directed Research and Development (LDRD) project at Sandia National Laboratories (SNL) and by the Science of Precision Multifunctional Nanostructures for Electrical Energy Storage (NEES), an Energy Frontier Research

Center funded by the U.S. Department of Energy (DOE), Office of Science, Office of Basic Energy Sciences (BES) under award DESC0001160. This work was performed in part at the Sandia-Los Alamos Center for Integrated Nanotechnologies (CINT), a U.S. DOE, Office of BES user facility. The LDRD supported the development and fabrication of platforms and the development of TEM techniques. The NEES center supported some of the additional platform development and fabrication and materials characterization. CINT supported the TEM capability and the fabrication capabilities that were used for the TEM characterization, and this work represents the efforts of several CINT users, primarily those with affiliation external to SNL. SNL is a multiprogram laboratory operated by Sandia Corporation, a wholly owned subsidiary of Lockheed Martin company, for the DOE's National Nuclear Security Administration under contract DE-AC04-94AL85000. The work of C.M.W. and W.X. was supported by the DOE Office of Science, Offices of Biological and Environmental Research, and was conducted in the Environmental Molecular Sciences Laboratory, a national scientific user facility sponsored by DOE's Office of Biological and Environmental Research and located at Pacific Northwest National Laboratory, which is operated by Battelle for the DOE under contract DE-AC05-76RLO1830. L.Q., A.K., and J.L. were supported by Honda Research Institute USA, Xi'an Jiaotong University, NSF grants CMMI-0728069, DMR-1008104, and DMR-0520020, and Air Force Office of Scientific Research grant FA9550-08-1-0325. S.X.M., L.Z., and L.Q.Z. were supported by NSF grants CMMI0825842 and CMMI0928517 through the University of Pittsburgh and SNL. L.Q.Z. thanks the Chinese Scholarship Council for financial support and Z. Ye's encouragement from Zhejiang University.

Supporting Online Material
www.sciencemag.org/cgi/content/full/330/6010/1515/DC1
Materials and Methods
Figs. S1 to S11
Movies S1 to S5
References

26 July 2010; accepted 26 October 2010
10.1126/science.1195628

Optomechanically Induced Transparency

Stefan Weis,[1,2]* Rémi Rivière,[2]* Samuel Deléglise,[1,2]* Emanuel Gavartin,[1] Olivier Arcizet,[3] Albert Schliesser,[1,2] Tobias J. Kippenberg[1,2]†

Electromagnetically induced transparency is a quantum interference effect observed in atoms and molecules, in which the optical response of an atomic medium is controlled by an electromagnetic field. We demonstrated a form of induced transparency enabled by radiation-pressure coupling of an optical and a mechanical mode. A control optical beam tuned to a sideband transition of a micro-optomechanical system leads to destructive interference for the excitation of an intracavity probe field, inducing a tunable transparency window for the probe beam. Optomechanically induced transparency may be used for slowing and on-chip storage of light pulses via microfabricated optomechanical arrays.

Coherent interaction of laser radiation with multilevel atoms and molecules can lead to quantum interference in the electronic excitation pathways (*1*). A prominent example observed in atomic three-level systems is the phenomenon of electromagnetically induced transparency (EIT), in which a control laser induces a narrow spectral transparency window for a weak probe laser beam. When this generic EIT effect had first been observed in an atomic gas (*2*), its relevance in nonlinear optics and optical (quantum) information processing was quickly recognized. In particular, the rapid variation of the refractive index concomitant with the opening of the transparency window gives rise to a dramatic reduction of the group velocity of a propagating optical pulse (*3*, *4*). Dynamic control of EIT with the control laser enables even a complete stop, that is, storage, of the pulse in an atomic medium (*5*, *6*). The experimental demonstration of slowing and stopping light (*3*–*6*) has attracted strong attention, because it provides a route to implement a photonic quantum memory (*7*) or a classical optical buffer. EIT has subsequently been studied in a wide variety of atomic media, but also in several solid-state systems (*8*, *9*) with a well-suited level structure.

Recent experiments with optomechanical systems have demonstrated that the mechanical response to thermal forces can be controlled by an optical field. This effect has been exploited, for example, to implement optomechanical laser cooling and amplification (*10*–*13*) as well as normal mode splitting (*14*). In other work, the mechanical response was optically tailored to exhibit destructive interference between different mechanical excitation pathways (*15*). Whereas in these studies, the mechanical response to thermal Langevin force was modified, we demonstrate here, as recently suggested (*16*, *17*), that the system's optical response to a weak "probe" laser can be controlled by a second "control" laser driving the lower motional sideband. A window of transparency arises from the destructive interference of excitation pathways for the intracavity probe field when a two-photon resonance condition is met. As pointed out independently, this effect can be considered a strict optomechanical analog of EIT (*18*), originating from a similar effective interaction Hamiltonian (*19*). Advantageously, this form of induced transparency does not rely on naturally occurring resonances and could therefore also be applied to previously inaccessible wavelength regions such as the technologically important near-infrared. Furthermore, a single optomechanical element can already achieve unity contrast, which in the atomic case is only possible within the setting of cavity quantum electrodynamics (*20*).

Our experiment (Fig. 1) consists of an optomechanical system featuring linear optomechanical coupling G in the sense that the cavity resonance frequency is given by $\omega_c'(x) = \omega_c + Gx$, where ω_c is the unperturbed resonance frequency. A control laser (frequency ω_l) maintains a control field $\bar{a}e^{-i\omega_l t}$, containing $|\bar{a}|^2$ photons, in the cavity. The static radiation pressure originating from this field displaces the mechanical mode by $\bar{x}$, leading to an effective detuning from the cavity resonance $\bar{\Delta} = \omega_l - (\omega_c + G\bar{x})$. We consider the situation where the control laser is tuned close to the lower motional sideband, i.e., $\bar{\Delta} \approx -\Omega_m$, where Ω_m is the mechanical (angular) resonance frequency. A second, weak laser oscillating at $\omega_p = \omega_l + \Omega$, is subsequently used to probe the (modified) cavity resonance by driving an intracavity probe field contained in a perturbation term $\delta a(t)$.

In the case of a weak probe field (compared to the control field), one can linearize the optomechanical dynamics (*21*) for the mechanical displacement $x(t) = \bar{x} + \delta x(t)$ and the intracavity field $a(t) = [\bar{a} + \delta a(t)]e^{-i\omega_l t}$ around the steady-state values $(\bar{x}, \bar{a})$. For the probe power transmission—that is, the ratio of the probe power returned from the system divided by the input probe power—the general expression

$$|t_p|^2 = \left| 1 - \frac{1 + if(\Omega)}{-i(\bar{\Delta} + \Omega) + \kappa/2 + 2\bar{\Delta}f(\Omega)} \eta_c \kappa \right|^2 \quad (1)$$

with

$$f(\Omega) = \hbar G^2 \bar{a}^2 \; \frac{\chi(\Omega)}{i(\bar{\Delta} - \Omega) + \kappa/2} \quad (2)$$

can be derived [see (*16*–*18*) and supporting online material (SOM) Eq. S25]. Here, $\chi(\Omega) = [m_{\mathrm{eff}}(\Omega_m^2 - \Omega^2 - i\Gamma_m\Omega)]^{-1}$ is the susceptibility of the mechanical oscillator of effective mass m_{eff} and damping rate Γ_m. The optical mode is characterized by a total loss rate $\kappa = \kappa_0 + \kappa_{ex}$ and the cavity coupling parameter $\eta_c = \kappa_{ex}/(\kappa_0 + \kappa_{ex})$. The presence of a control field $\bar{a}$ (tuned to the lower sideband) induces a transmission window for the probe beam when the resonance condition $\Omega \approx \Omega_m$ is met (Fig. 1). The depth and the width of this transmission window are tunable by the power of the control beam, as in the case of atomic EIT, with the best contrast achieved in the case of critical coupling $\eta_c = 1/2$.

To gain more physical insight into this phenomenon, it is instructive to consider this effect in a sideband picture. The simultaneous presence of control and probe fields generates a radiation-

[1]Ecole Polytechnique Fédérale de Lausanne, EPFL, 1015 Lausanne, Switzerland. [2]Max-Planck-Institut für Quantenoptik, Hans-Kopfermann-Strasse 1, 85748 Garching, Germany. [3]Institut Néél, 25 Rue des Martyrs, 38042 Grenoble, France.

*These authors contributed equally to this work.
†To whom correspondence should be addressed. E-mail: tobias.kippenberg@epfl.ch